Volume 4
Number 2
March 2026
Pages 241–486

EES Catalysis

rsc.li/EESCatalysis

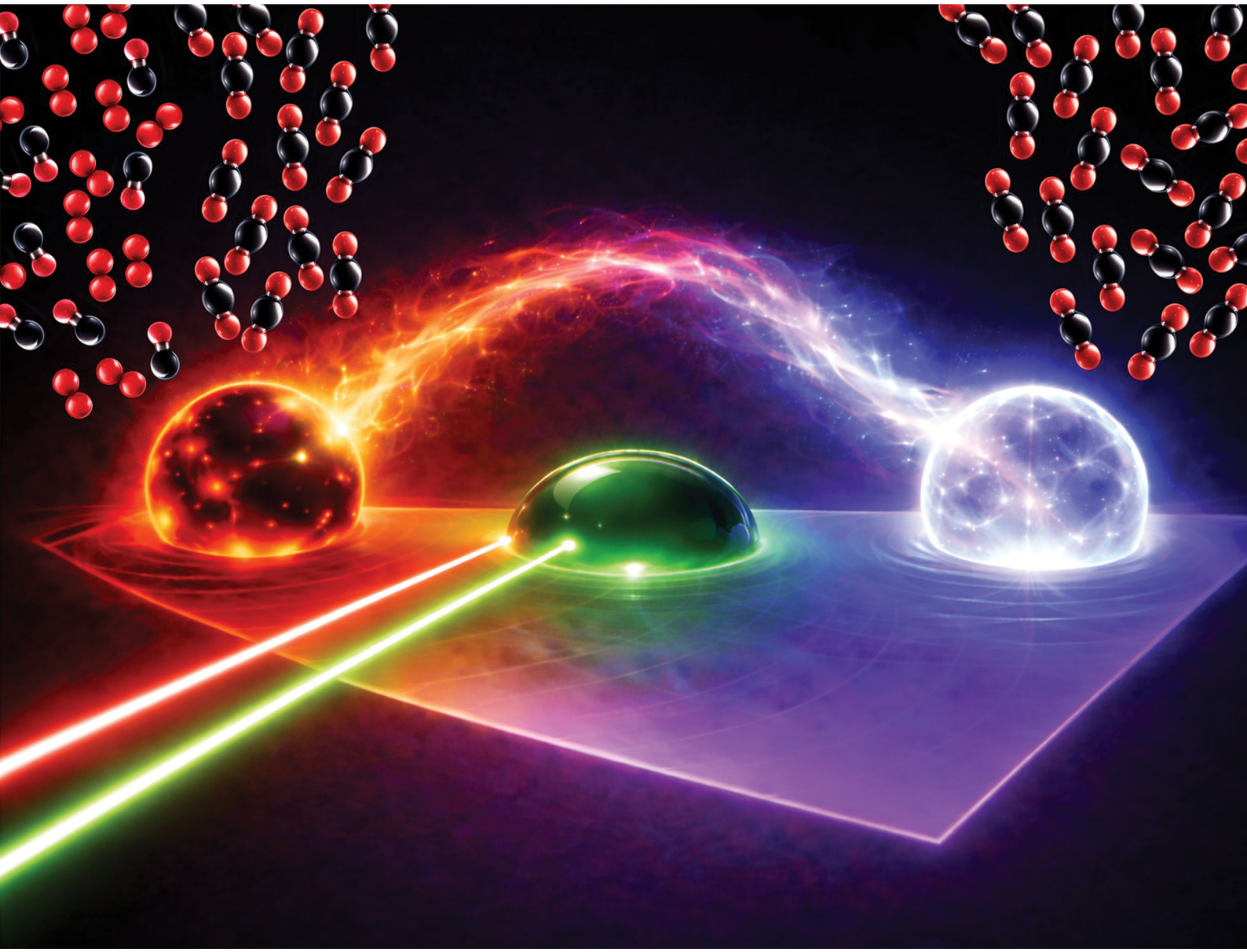

ISSN 2753-801X

ROYAL SOCIETY OF CHEMISTRY

COMMUNICATION
Andrea D. Pickel, Marc D. Porosoff *et al.*
Leveraging and understanding exotherms in tandem catalysts with *in situ* luminescence thermometry

EES Catalysis

COMMUNICATION

View Article Online
View Journal | View Issue

Cite this: *EES Catal.*, 2026, 4, 333

Received 7th November 2025,
Accepted 14th December 2025

DOI: 10.1039/d5ey00319a

rsc.li/eescatalysis

Leveraging and understanding exotherms in tandem catalysts with *in situ* luminescence thermometry

Sinhara M. H. D. Perera, [a] Benjamin Harrington, [b] Adel Fadhul,[a] Andrea D. Pickel *[c] and Marc D. Porosoff *[a]

Leveraging thermal gradients on catalyst surfaces remains largely underexplored despite their profound effects on reaction kinetics. In this work, we use upconverting nanoparticle (UCNP)-based luminescence thermometry to directly measure catalyst surface temperatures under *in situ* conditions during thermally coupled tandem reactions. Using UCNPs loaded on a model dual-functional material (DFM), Pt–CaO/CeO_2, we observe hot spots of ~10–100 °C above the bulk bed temperature during exothermic CO oxidation. Isotopically labeled $^{13}CO_2$ diffuse reflectance infrared Fourier transform spectroscopy (DRIFTS) supports our hypothesis that reaction-generated heat drives endothermic CO_2 desorption from CaO. Proximity studies show that nanoscale co-localization of Pt and CaO improves thermal coupling relative to dual-bed configurations, highlighting the importance of spatial organization. Comparison of UCNP thermometry with thermocouple readings further demonstrates that bulk temperature measurements underestimate true surface temperatures during exothermic reactions, underscoring the critical role of probe placement for accurate kinetic evaluation. Our methodology opens new avenues for accurate kinetic analysis, *in situ* thermal profiling, and rational design of thermally integrated tandem catalysts and DFMs, with direct implications for more complex transformations such as CO_2 hydrogenation.

Broader context

Catalytic processes underpin the synthesis of chemicals and fuels that are necessary for modern society, but the actual temperatures of catalytic surfaces during reactions are quite different from the "bulk" values we measure and use to make decisions. The micro/nano-scale hot spots and thermal gradients can waste energy, distort reported kinetics measurements, and lead to suboptimal materials or reactor designs. This study demonstrates how we can understand and leverage thermal gradients on a catalyst surface during an exothermic reaction to drive an endothermic step in a dual-functional material designed for CO_2 capture and conversion. The results demonstrate the importance of catalyst design in reducing the external heating load to improve overall energy efficiency. Our study also clarifies why thermocouple probe placement and catalyst bed configuration are critical for accurately measuring reaction rates. Because many carbon management chemistries such as CO_2 capture and conversion pair endo- and exothermic steps, the ability to quantify and engineer nanoscale thermal coupling offers an important lever to lower energy demand and design improved catalysts.

1. Introduction

Tandem catalysts contain multiple distinct active sites to direct reactants through a series of precise transformations to selectively produce desired products. These complex catalysts streamline chemical transformations that typically require separate catalysts and/or reactors, thereby increasing energy efficiency *via* process intensification.[1–3] Tandem catalysts have been used extensively for conversion of small molecules into value-added chemicals and fuels, and upcycling of plastic waste into olefins and aromatics.[4–6] One well-studied example is CO_2 hydrogenation *via* the CO-mediated route, where CO_2 is first converted into CO *via* endothermic reverse water-gas shift (RWGS; $CO_2 + H_2 \rightleftharpoons CO + H_2O$; $\Delta_R H_{298\,K}^0 = 42.1$ kJ mol^{-1}), which in turn diffuses to secondary active sites where CO is converted to value-added hydrocarbons *via* exothermic Fischer–Tropsch synthesis (FTS; $CO + 2H_2 \rightarrow (-CH_2)- + H_2O$; $\Delta_R H_{298\,K}^0 = -152.0$ kJ mol^{-1}).[2]

[a] *Department of Chemical and Sustainability Engineering, University of Rochester, Rochester, NY 14627, USA. E-mail: marc.porosoff@rochester.edu*
[b] *Materials Science Program, University of Rochester, Rochester, NY 14627, USA*
[c] *Department of Mechanical Engineering, University of Rochester, Rochester, NY 14627, USA. E-mail: apickel@UR.Rochester.edu*

Although mass transfer of intermediates, *e.g.*, CO, in tandem catalysts has been well-studied by tuning the proximity of active components, the role of local thermal environments on the reaction mechanism remains largely overlooked.[3,7–10] This is in part because during typical kinetic measurements of heterogeneous catalysts, heat transfer limitations are avoided since they lead to ''false kinetics,'' where the actual temperature of the catalyst surface is significantly higher/lower than the measured bulk temperature of the catalyst bed.[11–14] For accurate and high-quality kinetic measurements, extensive reaction controls are required to maintain isothermal conditions and low conversion levels. For example, catalyst beds are typically diluted with high thermal conductivity silicon carbide (SiC) to mitigate heat and mass transfer effects that may lead to misleading kinetic measurements.[15–18]

In this work, we couple exo- and endothermic reactions over a model tandem catalyst to demonstrate increased energy efficiency of the overall process. Coupling exo- and endothermic reactions has been done at the macroscopic (reactor) scale, but the effect of thermal environments on the micro/nano scale, and specifically how thermal gradients affect elementary reaction steps, remains underexplored.[19–22] Furthermore, we illustrate how conducting reactions in commonly used experimental apparatuses for *in situ* X-ray absorption fine structure (XAFS) and diffuse reflectance infrared Fourier transform (DRIFTS) experiments can lead to significant temperature gradients that affect the validity of kinetic measurements.

2. Demonstrating thermal coupling

To better understand thermal gradients in tandem catalysts, we have selected a model system that uses 1.5 wt% Pt and 5 wt% CaO on a CeO_2 support (see SI, Section S1 for the synthesis procedure) to couple exothermic CO oxidation ($CO + \frac{1}{2}O_2 \rightarrow CO_2$; $\Delta_R H_{298\,K}{}^0 = -283.0$ kJ mol^{-1}) with endothermic CO_2 desorption ($CaCO_3 \rightarrow CaO + CO_2$; $\Delta_R H_{298\,K}{}^0 = +178.3$ kJ mol^{-1}). We have selected these two coupled reactions as a model for dual functional materials (DFMs), a class of tandem catalysts that combine CO_2 capture with CO_2 hydrogenation. In our study, we are simplifying the typical DFM system by using CO oxidation as a surrogate for exothermic CO_2 hydrogenation for its simplicity and lack of water byproduct that can complicate mass balances, product quantification, and heat transfer *via* condensation. Additionally, our system spatially decouples the heat sink (CO_2 desorption sites on CaO), from the heat source (CO oxidation sites on Pt). The choice of Pt supported on CeO_2 for CO oxidation synthesized with a tetraammineplatinum(II) nitrate (TAPN) precursor is based on prior literature, indicating it is a well-established, active, and stable low-temperature CO oxidation catalyst.[23,24] Therefore, coupling CO oxidation with CO_2 desorption over the Pt–CaO/CeO_2 DFM enables us to limit the number of confounding variables and carefully probe energy efficiency and discrepancies between bulk and local temperatures.

To provide clear evidence that the CO oxidation exotherm directly drives endothermic CO_2 desorption from CaO, we first perform DRIFTS experiments on the Pt–CaO/CeO_2 DFM with pre-adsorbed, isotopically labeled $^{13}CO_2$ to distinguish between the CO_2 that is produced *via* CO oxidation and the desorbing CO_2 that is pre-adsorbed on CaO. The gas-phase $^{12}CO_2$ produced during CO oxidation and pre-adsorbed $^{13}CO_2$ exhibit distinct asymmetric stretching (ν_3) vibrational modes, enabling isotopic discrimination *via* infrared spectroscopy.

In the DRIFTS experiments, we first saturate the surface of Pt–CaO/CeO_2 with $^{13}CO_2$, followed by inert purging in N_2 to remove physisorbed species, and then we introduce a flow of $^{12}CO/O_2$ at 150 °C (see SI, Section S2 for detailed methodology). While partial spectral overlap occurs between the P-branch of $^{12}CO_2$ and the R-branch of $^{13}CO_2$ in the 2290–2320 cm^{-1} region, the R-branch of the $^{12}CO_2$ ν_3 mode and the P-branch of the $^{13}CO_2$ ν_3 mode remain well resolved (Fig. 1a). This separation enables accurate identification and quantification of each isotope of CO_2, such that we can discern between desorbing CO_2 ($^{13}CO_2$) and CO_2 produced during CO oxidation ($^{12}CO_2$).

Following introduction of the $^{12}CO/O_2$ mixture under isothermal conditions at 150 °C, we observe a sharp increase in gas-phase $^{13}CO_2$ desorbing from the surface, alongside newly formed gas-phase $^{12}CO_2$ and chemisorbed ^{12}CO (Fig. 1b and c). The simultaneous evolution of both isotopes of CO_2 strongly suggests that the endothermic desorption of $^{13}CO_2$ is thermally driven by the heat released from exothermic ^{12}CO oxidation. Fig. 1d further supports our claim of thermally coupled endo- and exothermic processes *via* the continuous increase in $^{13}CO_2$ desorption that mirrors the production of gas-phase $^{12}CO_2$. The $^{13}CO_2$ signal peaks at approximately 15 minutes and gradually declines as the surface reservoir of chemisorbed $^{13}CO_2$ becomes depleted, underscoring the role of reaction-generated heat in sustaining CO_2 desorption. This observation is in stark contrast to the control experiment under N_2 at 150 °C where no $^{13}CO_2$ desorption is observed. Collectively, the DRIFTS results provide compelling evidence that the thermal energy released during CO oxidation directly drives CO_2 desorption, demonstrating the importance of thermal coupling for designing more efficient DFMs.

To better quantify the effect of thermal coupling on external heating requirements and energy efficiency, we performed an analysis comparing thermally coupled CO oxidation-driven CO_2 desorption with the uncoupled case in which CO_2 desorption occurs solely through external heating (refer to SI, Section S3 for the detailed methodology). Comparative experiments with and without pre-adsorbed CO_2 on Pt–CaO/CeO_2 in a 1 mm quartz capillary reactor mounted within a custom-designed Clausen cell show that pre-adsorbed CO_2 is desorbed during isothermal CO oxidation at 100 °C, indicating that locally generated heat from the exothermic reaction directly drives CO_2 release from the CaO adsorbent. Mass balance analysis (refer to SI, Section S3 and Fig. S1–S3 and Table S1) reveals that ~27% of the chemisorbed CO_2 is desorbed due to the CO oxidation exotherm, while requiring significantly less external heat. These results provide proof-of-concept evidence that

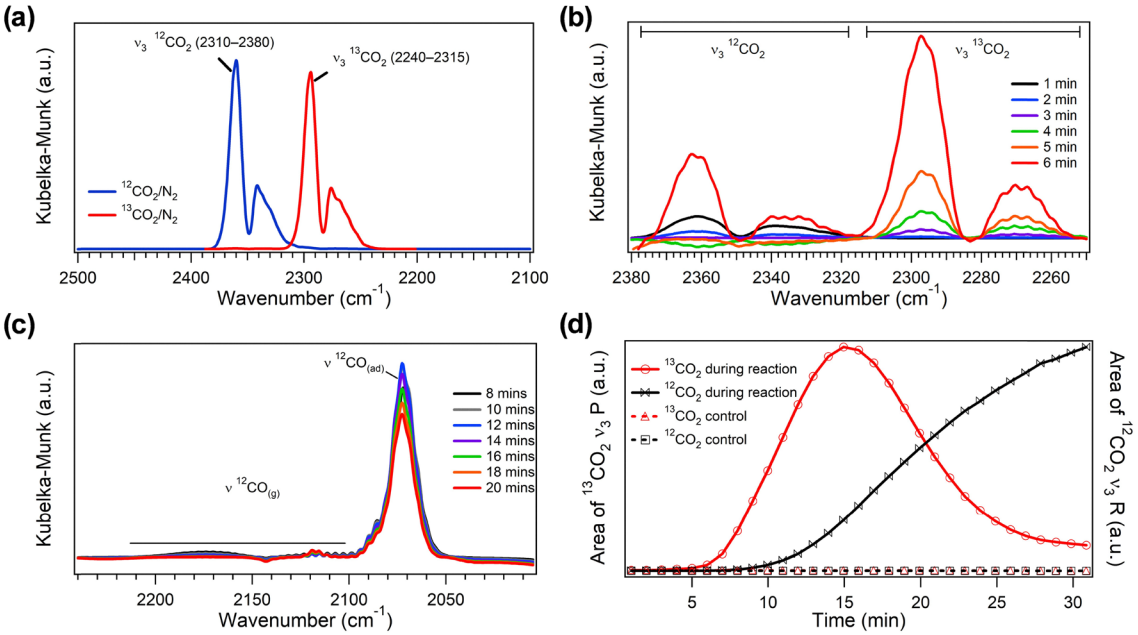

Fig. 1 $^{13}CO_2$ isotopic labeling experiment demonstrating CO oxidation-driven CO_2 desorption from CaO. (a) DRIFTS spectra of isotopic CO_2/N_2 gas mixtures referenced to pure N_2 background, highlighting the asymmetric stretching (ν_3) vibrational modes of CO_2. Blue: $^{12}CO_2/N_2$; red: $^{13}CO_2/N_2$. (b) Evolution of the ν_3 bands of $^{13}CO_2$ and $^{12}CO_2$ during the first 6 minutes after introducing $^{12}CO/O_2$ under isothermal conditions at 150 °C, showing desorption of chemisorbed $^{13}CO_2$ concurrent with ^{12}CO oxidation. (c) Time-resolved profiles of gas-phase and chemisorbed ^{12}CO species following $^{12}CO/O_2$ introduction, highlighting reaction progress at the DFM surface. (d) Temporal comparison of peak areas for the $^{13}CO_2$ ν_3 P-branch and the $^{12}CO_2$ ν_3 R-branch, contrasting the CO oxidation reaction with a control experiment conducted under non-reactive N_2 at 150 °C.

coupling exothermic and endothermic steps can reduce external heating requirements, and potentially increase the overall energy efficiency of catalytic processes.

3. Quantifying temperature gradients with UCNPs

The above results demonstrate that thermal coupling reduces external heating requirements. However, elucidating the underlying mechanism requires direct measurement of local temperature gradients on the catalyst surface under *in situ* reaction conditions. To help bridge this knowledge gap, we have developed an approach that uses luminescence thermometry, specifically ratiometric thermometry *via* upconverting nanoparticles (UCNPs), for spatially resolving the temperature of the catalyst surface. We designed a Clausen cell with a quartz capillary reactor mounted on a custom-built scanning confocal microscope to quantify the discrepancy between the average "bulk" temperature of the catalyst bed and the actual temperature of the surface during coupled CO oxidation-CO_2 desorption.[25] Here, the bulk temperature of the catalyst bed is defined as the temperature of the gas phase flowing through the interstitial voids between and within catalyst particles and not the internal bulk temperature of the individual catalyst particles. For measuring the bulk temperature, a thermocouple is in contact with the boundary of the catalyst bed, representing a cross-sectional average of the gas-phase temperature at the location of the probe (Fig. 2a).[26]

For measuring the surface temperature, we use ratiometric thermometry *via* UCNPs, a technique that has gained increasing attention as a tool for probing localized temperature gradients under *in situ* reaction conditions (Fig. 2b).[27–31] While infrared thermography enables remote monitoring of catalyst surface temperatures, our approach provides higher spatial resolution and does not require knowledge of the catalyst surface emissivity, which is often challenging to determine experimentally and can also evolve dynamically during catalytic processes.[32] The UCNP ratiometric thermometry signal relies on the relative emission intensities originating from two thermally coupled electronic states whose populations follow Boltzmann statistics. UCNP-based ratiometric thermometry minimizes artifacts due to fluctuations in the excitation intensity or light collection efficiency, and is independent of the concentration or dispersion of the probe material, with spatial resolution ultimately limited by optical diffraction.[28,32,33] The UCNPs in this study are composed of a $NaYF_4$ host matrix doped with Yb^{3+} and Er^{3+} ions, and are embedded within the catalyst architecture, denoted as UCNP-Pt–CaO/CeO_2, to enable spatially resolved local temperature measurements under *in situ* reaction conditions. The underlying working principle of UCNP-based thermometry (Fig. S4, SI, Section S4) and the synthesis protocol of the UCNP-Pt–CaO/CeO_2 DFMs are detailed in the SI, Section S1.

Transmission electron microscopy (TEM) of UCNP-Pt–CaO/CeO_2 (Fig. 2c and Fig. S5) reveals that the UCNPs possess a well-defined crystalline structure with a characteristic hexagonal platelet morphology and an average particle diameter of

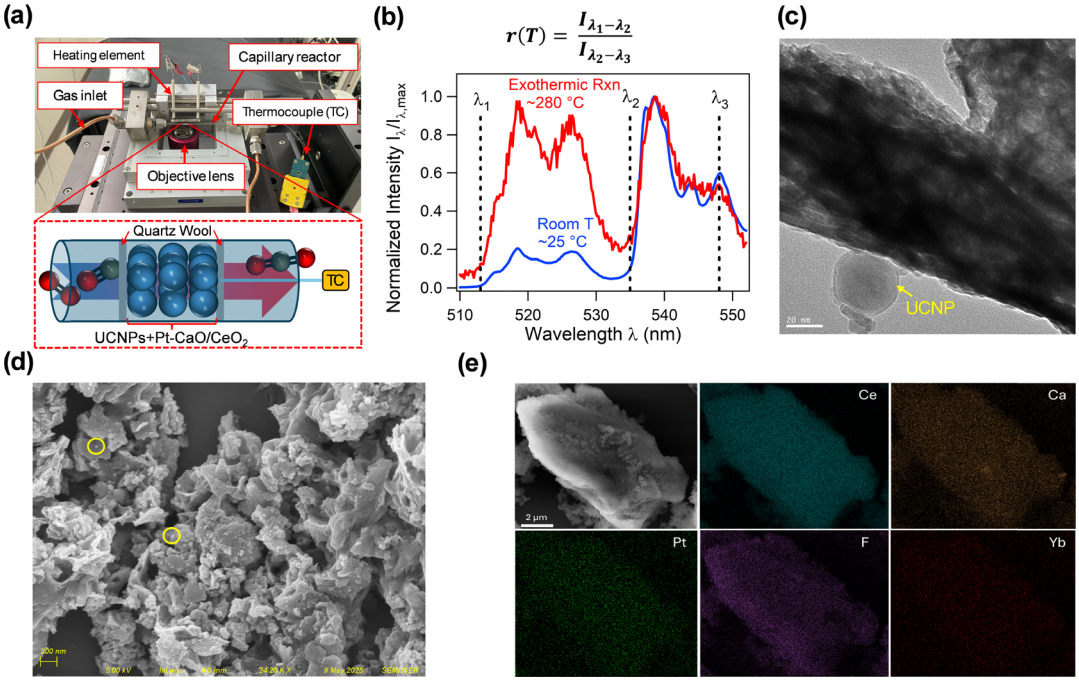

Fig. 2 (a) The experimental setup showing the Clausen cell mounted on the confocal microscope for *in situ* luminescence thermometry, accompanied by a schematic indicating the placement of the thermocouple within the DFM bed. (b) Representative luminescence spectra of $NaYF_4$:Yb^{3+},Er^{3+} UCNPs recorded at 25 °C and 280 °C, illustrating the thermometric principle based on temperature-dependent emission intensity ratios. (c) TEM image of UCNP-Pt–CaO/CeO_2 showing an individual UCNP on the catalyst surface at 20 nm scale. (d) SEM image displaying the overall DFM morphology, with UCNPs uniformly dispersed across the surface (selected UCNPs are circled in yellow to guide the eye). (e) SEM-EDS elemental mapping confirming the homogeneous distribution of all major components: UCNPs (Yb, F), Pt, CaO, and CeO_2.

~30 nm. For detailed descriptions of the catalyst characterization techniques, refer to the SI, Section S5. As shown in Fig. S6, TEM imaging further confirms Pt is well-dispersed, with dark contrast regions attributed to Pt (Z = 78) due to the higher atomic number relative to Ce, Ca, and the UCNP matrix. Scanning electron microscopy (SEM) images in Fig. 2d highlight the overall catalyst morphology, showing ~30 nm UCNPs uniformly distributed across the DFM surface. Additionally, SEM-energy dispersive X-ray spectroscopy (SEM-EDS) mapping (Fig. 2e) supports the homogeneous spatial distribution of all key components (UCNPs, Pt, and CaO) on the CeO_2 support.

To measure the temperature of the UCNPs during *in situ* experiments, the setup in Fig. 2a features a 976 nm laser for UCNP excitation, a manual micropositioning stage, a piezo-controlled nanopositioning stage, an avalanche photodiode for luminescence intensity detection, a spectrometer coupled with a CCD camera for spectral acquisition, and a LI-COR gas analyzer for quantifying downstream CO_2 concentration. Additional details of the UCNP-based luminescence apparatus and temperature calibration of the UCNPs are included in the SI, Section S6 and Fig. S7.

As we have already demonstrated the importance of thermal coupling during DRIFTS experiments in Fig. 1, our first application of the UCNP measurements is to better understand the effect of proximity of catalytic components on heat transfer. During investigations of tandem catalysts, many studies report proximity effects in the context of mass transfer of intermediates, which is known to greatly affect the kinetics of tandem reactions.[34,35] However, studies generally do not consider proximity effects in the context of heat transfer, which may also affect the efficiency of tandem reactions.

To investigate proximity effects, we conducted experiments with preadsorbed CO_2 using a dual-bed DFM composed of UCNP-Pt/CeO_2 and UCNP-CaO/CeO_2 separated by quartz wool in the Clausen cell (refer to SI, Section S7 for the detailed experimental procedure). In contrast to the Pt–CaO/CeO_2 co-impregnated DFM, where the active Pt sites (hot reactive centers) and CaO (heat sinks during CO_2 desorption) are in nanoscale proximity, the dual-bed configuration spatially separates Pt/CeO_2 and CaO/CeO_2 by millimeters. This stark contrast in length scales enables us to investigate how the spatial arrangement of DFM components affects thermal coupling of exo- and endothermic reactions.

Fig. 3a shows that the surface temperature of Pt/CeO_2 in the dual-bed configuration during reaction relative to the thermocouple (TC) reading (ΔT_{dual}) is significantly higher than that of the co-impregnated catalyst relative to its corresponding TC reading (ΔT_{coimp}). Even at low conversions (1.5–2%), ΔT_{dual} exceeds ΔT_{coimp} by approximately 18 °C, highlighting the critical role of proximity between Pt/CeO_2 reaction centers and CaO/CeO_2 heat sinks. In the co-impregnated DFM, the nanoscale proximity of Pt and CaO enables efficient thermal coupling of the exothermic CO oxidation reaction with endothermic CO_2 desorption, because the heat generated from

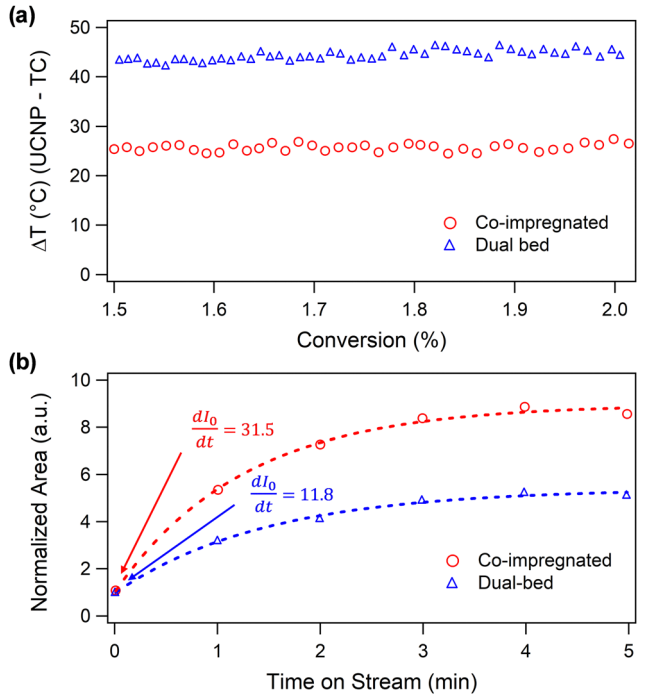

Fig. 3 Effect of DFM component proximity on thermal coupling between exothermic and endothermic reactions. (a) DFM surface temperature measured by UCNP thermometry under mild reaction conditions (1.5–2% conversion) for the co-impregnated DFM and the dual-bed configuration. The surface temperatures of the Pt/CeO_2 (red circles) in the dual-bed configuration and the co-impregnated DFM (blue triangles), relative to their respective thermocouple (TC) reading, are plotted against conversion. (b) Comparison of the initial rate of $^{13}CO_2$ desorption during exothermic ^{12}CO oxidation at 150 °C for the co-impregnated and dual-bed DFMs measured by DRIFTS. The normalized area of the P-branch of the $^{13}CO_2$ ν_3 band (I_0) is plotted against time-on-stream under reaction conditions, and the initial rate of change of the peak area (dI_0/dt) is calculated at t = 0 and is directly proportional to the initial rate of $^{13}CO_2$ desorption. The experimental data were fitted using an exponential function of the form $k_0 + k_1 \exp(-k_3 x)$, where k_0, k_1, and k_2 are constants.

the exothermic reaction on Pt travels less distance before being consumed during endothermic desorption of CO_2 from CaO. In comparing the co-impregnated *versus* dual-bed scenarios, the extreme difference in spatial proximity between the catalytic and adsorbent sites ensures that the resulting difference in the measured temperature rises can unambiguously be attributed to this spatial proximity difference, rather than simply resulting from spatial temperature heterogeneity. In the future, temperature mapping studies that better capture temperature heterogeneities within the catalyst bed could facilitate improved comparisons among different spatial orientations of active sites, including physical mixing.

To further support our findings regarding the importance of proximity in thermally coupling exo- and endothermic reactions, we conducted a DRIFTS experiment to compare the initial rate of CO_2 desorption driven by CO oxidation in co-impregnated and dual-bed DFMs with pre-adsorbed $^{13}CO_2$ (Refer to SI, Section S8 for the detailed experimental procedure). The sample is first degassed under N_2 at 400 °C for 1 h and subsequently saturated with $^{13}CO_2$ at 25 °C. It is then purged under N_2 at 150 °C to remove physisorbed $^{13}CO_2$ before introducing the $^{12}CO/O_2$ reactant mixture at 150 °C. The initial desorption rate of $^{13}CO_2$ is determined from the rate of increase in the peak area of the gas-phase $^{13}CO_2$ ν_3 band at t = 0 min (eqn (S4–S6 in SI, Section S8). To minimize errors arising from partial overlap between the $^{13}CO_2$ and $^{12}CO_2$ ν_3 bands, the peak area is quantified exclusively from the P-branch of the $^{13}CO_2$ ν_3 band (Fig. S8). As shown in Fig. 3b, the initial rate of $^{13}CO_2$ desorption for the co-impregnated DFM, where the components are in nanoscale proximity, is approximately 2.7 times that of the dual-bed DFM, where the components are stacked, demonstrating closer proximity of the DFM components increases the thermal efficiency of coupling exo- and endothermic reactions.

We also conducted isotopically labeled DRIFTS experiments at 150 °C while varying the Pt : CaO mass ratio (0.1, 0.3, and 0.6) in the co-impregnated DFM to investigate the effect of the relative abundance of Pt and CaO sites. As shown in Fig. S9, the results indicate an optimal Pt : CaO mass ratio that maximizes thermal coupling, evidenced by the highest initial $^{13}CO_2$ desorption rate. This confirms that the relative abundances of sites responsible for the exothermic reaction (heat source) and those mediating the endothermic reaction (heat sink) directly influence the degree of thermal coupling.

4. Consequences of inaccurate temperature measurements

Because proximity effects and temperature gradients are evident during thermal coupling over Pt–CaO/CeO_2, we leveraged our unique experimental setup to directly probe the consequences of inaccurate temperature measurements under *in situ* conditions. To understand thermal heterogeneities within the catalyst bed during CO oxidation, we quantified the temperature difference between localized regions of the DFM surface, measured *via* UCNPs, and the temperature recorded by a thermocouple positioned either in direct contact with the DFM bed or in the quartz wool at the bed boundary in our custom-designed Clausen cell.

For the CO oxidation experiments with the thermocouple in direct contact with the DFM bed (Fig. 4a), ~2 mg of UCNP-Pt–CaO/CeO_2 is loaded into the 1 mm quartz capillary, and a temperature-programmed reaction is carried out under 10 mL min^{-1} of 9 vol% CO/4.5 vol% O_2/balance N_2, as detailed in the SI, Section S7. A control experiment is performed under an inert 10 mL min^{-1} N_2 flow with the same temperature profile to isolate thermal effects arising from the CO oxidation reaction.

The temperature comparison between the UCNPs and the thermocouple shows the expected result that localized thermal gradients are a direct consequence of the exothermic CO oxidation reaction, clearly demonstrating the importance of accounting for heat transfer limitations when measuring catalyst kinetics. As detailed in Fig. 4a, the DFM surface temperature during the reaction measured *via* UCNP-based

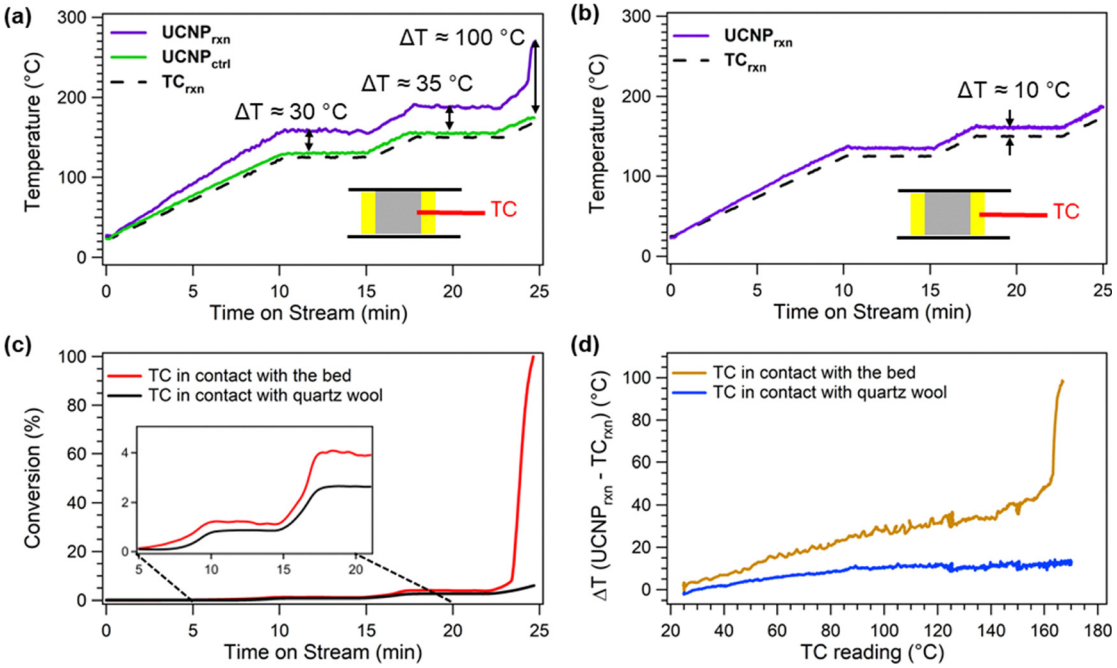

Fig. 4 Catalyst surface temperature measured by UCNP-based luminescence thermometry compared with the bulk temperature recorded by a thermocouple in contact with the (a) catalyst bed and (b) quartz wool, during CO oxidation over UCNP-Pt–CaO/CeO_2. (c) Corresponding CO conversion profile under reactive conditions. (d) Corresponding surface *vs.* TC temperature difference during the temperature-programmed CO oxidation reaction plotted against the temperature recorded by the TC. Time on stream denotes time after beginning the CO oxidation reaction. The TC temperature is tied to a feedback-controlled PID system that regulates the heating output.

thermometry ($UCNP_{rxn}$) is significantly higher than the bulk bed temperature recorded by the thermocouple in contact with the DFM bed (TC_{rxn}). Notably, the surface temperatures are approximately 35 °C, 40 °C, and 100 °C higher relative to the bulk temperature at ~1%, ~4%, and ~96% CO conversion, respectively. The control experiment under inert conditions reveals the surface temperature ($UCNP_{ctrl}$) closely tracks the thermocouple reading TC_{ctrl}, with the largest deviation of ~6 °C observed when TC_{ctrl} > 125 °C. This small difference observed during the control experiment under non-reactive conditions is attributed to a slight temperature gradient, arising from the marginally closer proximity of the DFM bed to the heating element relative to the thermocouple. We also note that TC_{ctrl} is within 2 °C of TC_{rxn}, even though the measurements are taken during separate experiments. The difference between TC_{ctrl} and TC_{rxn} is plotted in Fig. S10, and only one trace of the thermocouple data is included in Fig. 4a for clarity.

The observed temperature differences between $UCNP_{rxn}$ and TC_{rxn} in Fig. 4a likely result from thermal resistance across the boundary layer at the gas–solid interface, arising from the low thermal conductivity of both the catalyst bed and the gas stream.[36] Similar thermal gradients have been observed in simulations, where localized catalytic activity leads to hot spots that exceed bulk temperatures of the catalyst bed.[37,38] Furthermore, the heterogeneity of the catalyst bed combined with finite rates of heat conduction and convection prevent the bulk catalyst bed and surface temperatures from becoming equal.[36,39] Existing strategies to mitigate heat transfer limitations, such as increasing flow rates, reducing particle size, intraparticle/interparticle dilution, or employing dynamic temperature profiles, offer only partial solutions and carry their own trade-offs.[40] In contrast, our approach of directly measuring localized temperatures with UCNPs enables direct, real-time measurements of the actual surface temperature for precise kinetic analysis during exothermic reactions.

Importantly, especially for researchers who use Clausen cells or similar apparatuses for collecting XAFS data, the magnitude of the temperature difference between the DFM surface ($UCNP_{rxn}$) and the bulk temperature recorded by the thermocouple (TC_{rxn}) depends strongly on the thermocouple placement (*e.g.*, within the DFM bed *vs.* in contact with quartz wool at the bed boundary). This sensitivity arises because the thermocouple (TC) temperature is tied to a feedback-controlled PID system that regulates the heating output to maintain the set temperature. As shown in Fig. 4b and c, when the thermocouple is positioned in the quartz wool, the CO oxidation experiment exhibits smaller temperature differences (~10 °C at ~2% CO conversion) under otherwise identical reaction conditions. This discrepancy arises from the non-linear temperature gradient along the direction from the TC to the catalyst bed, determined by the relative positions of the bed and heating element with respect to the TC, and the resulting PID response to the temperature measured at the TC. When the TC contacts the catalyst bed, the PID loop delivers a higher output (Fig. S11), increasing the actual DFM temperature (Fig. 4a). When the TC is in contact with the quartz wool,

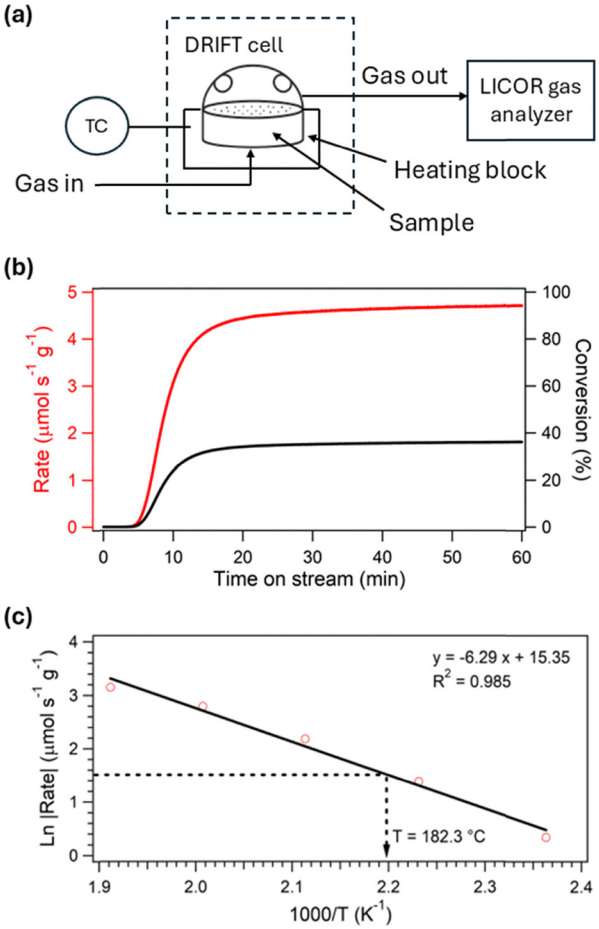

Fig. 5 (a) Schematic of the experimental design used to correlate DFM surface temperature with reaction rate. (b) Rate and conversion of isothermal CO oxidation at 150 °C (thermocouple reading) in a DRIFTS cell using the undiluted co-impregnated DFM (Pt–CaO/CeO_2). (c) Surface temperature *versus* rate calibration curve for the co-impregnated DFM (Pt–CaO/CeO_2). The calibration is performed using a 1:10 wt% DFM-to-KBr dilution to minimize thermal heterogeneities. Measurements are recorded at five set temperatures: 150, 175, 200, 225, and 250 °C. The plot also includes the estimated actual surface temperature of the DFM corresponding to isothermal CO oxidation at a thermocouple temperature of 150 °C (actual temperature is 181.9 °C). The raw data used to construct the calibration curve are provided in Fig. S13.

the lower actual temperature of the bed is a result of reduced power output by the temperature controller (Fig. 4b and Fig. S11). Because these experiments are conducted near the light-off region of CO oxidation (Fig. S12), we observe that the temperature gradients are amplified when the TC is embedded within the bed *versus* the quartz wool (Fig. 4d). These findings clearly demonstrate that millimeter-scale differences in thermocouple placement can introduce significant temperature discrepancies under reaction conditions and should therefore be carefully considered for accurately determining kinetic parameters.

We also conducted a DRIFTS experiment to demonstrate the significance of temperature heterogeneities in a Praying Mantis™ High Temperature Reaction Chamber during exothermic CO oxidation (Fig. 5a). In this experiment, the outlet gas stream from the DRIFTS cell was connected to a LI-COR CO_2 gas analyzer to correlate surface temperature with the reaction rate. We first generated a rate *versus* temperature calibration curve using a sample diluted with KBr at a 1 : 10 wt% DFM-to-KBr ratio to minimize thermal heterogeneities. Refer to the SI, Section S9, for detailed experimental procedures. Then, we conducted CO oxidation isothermally at a thermocouple reading of 150 °C on the undiluted co-impregnated DFM. Based on our measured reaction rate, the actual surface temperature estimated from the calibration curve reaches 182.3 °C, representing a ~32 °C (at ~36% conversion) difference relative to the thermocouple reading (Fig. 5b and c). This result is consistent with the surface temperature spike (~100 °C) observed *via* luminescence thermometry at 97% conversion in Fig. 4a. Clearly, these temperature discrepancies could go unnoticed during DRIFTS experiments because the cell design contains the thermocouple within a heating block. We therefore expect that inconsistencies in reported kinetic parameters, reaction mechanisms, and catalytic structures collected during DRIFTS could be attributed to inaccurate temperature measurements.[41]

5. Conclusions

UCNP luminescence thermometry measurements provide direct, minimally invasive measurements of catalyst surface temperatures under reaction conditions, resolving ~10–100 °C hot spots that conventional bulk thermocouples do not detect, thereby improving kinetic accuracy and reproducibility. Isotopic DRIFTS experiments confirm that the CO oxidation exotherm drives $^{13}CO_2$ desorption from CaO, and proximity studies show that nanoscale co-localization of heat sources (Pt) and heat sinks (CaO) improve thermal coupling relative to dual-bed DFM configurations. Our findings indicate the importance of careful thermal management as a key lever for rational tandem catalyst design, with immediate relevance to complex reaction mechanisms such as DFMs for CO_2 capture and conversion, and CO_2 hydrogenation. We anticipate that integrating *in situ* microthermometry into catalyst testing will enable more accurate kinetic evaluations and guide the design of thermally integrated tandem catalysts with increased energy efficiency.

Author contributions

SMHDP: investigation, visualization, writing – original draft, writing – review & editing. BH: investigation, visualization, writing – original draft, writing – review & editing. AF: investigation, ADP: supervision, project administration, funding acquisition, writing – review & editing. MDP: conceptualization, supervision, project administration, funding acquisition, writing – review & editing.

Conflicts of interest

There are no conflicts to declare.

Data availability

The data supporting this article have been included as part of the supplementary information (SI). Supplementary information is available. See DOI: https://doi.org/10.1039/d5ey00319a.

Acknowledgements

This work is supported by funding from Carbontech Development Initiative (Propel: 34820223) and is also supported in part by funding from the National Science Foundation (CBET-2345734). We thank Sean O'Neill of URnano, University of Rochester, for assistance with SEM measurements.

References

1 K. Takahashi, M. Yamashita and K. Nozaki, *J. Am. Chem. Soc.*, 2012, **134**, 18746–18757.
2 Z. Q. Ma and M. D. Porosoff, *ACS Catal.*, 2019, **9**, 2639–2656.
3 Y. Yamada, C. K. Tsung, W. Huang, Z. Huo, S. E. Habas, T. Soejima, C. E. Aliaga, G. A. Somorjai and P. Yang, *Nat. Chem.*, 2011, **3**, 372–376.
4 A. N. Biswas, L. R. Winter, Z. Xie and J. G. Chen, *JACS Au*, 2023, **3**, 293–305.
5 N. M. Wang, G. Strong, V. DaSilva, L. Gao, R. Huacuja, I. A. Konstantinov, M. S. Rosen, A. J. Nett, S. Ewart, R. Geyer, S. L. Scott and D. Guironnet, *J. Am. Chem. Soc.*, 2022, **144**, 18526–18531.
6 J. Sun, J. Dong, L. Gao, Y. Q. Zhao, H. Moon and S. L. Scott, *Chem. Rev.*, 2024, **124**, 9457–9579.
7 C. Xie, C. Chen, Y. Yu, J. Su, Y. Li, G. A. Somorjai and P. Yang, *Nano Lett.*, 2017, **17**, 3798–3802.
8 B. Shao, Z. Q. Wang, X. Q. Gong, H. Liu, F. Qian, P. Hu and J. Hu, *Nat. Commun.*, 2023, **14**, 996.
9 L. P. Merkouri, T. Ramirez Reina and M. S. Duyar, *Nanoscale*, 2022, **14**, 12620–12637.
10 I. S. Omodolor, H. O. Otor, J. A. Andonegui, B. J. Allen and A. C. Alba-Rubio, *Ind. Eng. Chem. Res.*, 2020, **59**, 17612–17631.
11 D. E. Mears, *Ind. Eng. Chem. Process Des. Dev.*, 1971, **10**, 541–547.
12 C. R. H. de Smet, M. H. J. M. de Croon, R. J. Berger, G. B. Marin and J. C. Schouten, *Appl. Catal., A*, 1999, **187**, 33–48.
13 L. Forni, *Catal. Today*, 1999, **52**, 147–152.
14 R. E. Hayes and S. T. Kolaczkowski, *Chem. Eng. Sci.*, 1994, **49**, 3587–3599.
15 B. J. P. Terlingen, T. Arens, T. P. van Swieten, F. T. Rabouw, P. T. Prins, M. M. de Beer, A. Meijerink, M. P. Ahr, E. M. Hutter, C. E. J. van Lare and B. M. Weckhuysen, *Angew. Chem., Int. Ed.*, 2022, **61**, e202211991.
16 F. H. Ribeiro, A. E. Schach Von Wittenau, C. H. Bartholomew and G. A. Somorjai, *Catal. Rev.*, 1997, **39**, 49–76.
17 G. Tuci, Y. Liu, A. Rossin, X. Guo, C. Pham, G. Giambastiani and C. Pham-Huu, *Chem. Rev.*, 2021, **121**, 10559–10665.
18 M. A. Vannice, *Kinetics of Catalytic Reactions*, 2005.
19 X. Ding, Z. Zhang, J. Sun, J. Y. Y. Loh, D. Ji, J. Lu, C. Liu, L. Zhao, W. Liu, J. Zhao, S. Tang, M. Safari, H. Cai, W. Tu, N. P. Kherani, Z. Hu, G. A. Ozin, Z. Zou and L. Wang, *Joule*, 2023, **7**, 2318–2334.
20 J. Wei, Q. Ge, R. Yao, Z. Wen, C. Fang, L. Guo, H. Xu and J. Sun, *Nat. Commun.*, 2017, **8**, 15174.
21 R. C. Ramaswamy, P. A. Ramachandran and M. P. Dudukovic, *Chem. Eng. Sci.*, 2008, **63**, 1654–1667.
22 F. X. Yin, S. F. Ji, H. Mei, Z. L. Zhou and C. Y. Li, *Chem. Eng. J.*, 2009, **155**, 285–291.
23 L. Nie, D. Mei, H. Xiong, B. Peng, Z. Ren, X. I. P. Hernandez, A. DeLaRiva, M. Wang, M. H. Engelhard, L. Kovarik, A. K. Datye and Y. Wang, *Science*, 2017, **358**, 1419–1423.
24 B. Bohigues, S. Rojas-Buzo, D. Salusso, Y. Xia, A. Corma, S. Bordiga, M. Boronat, T. Willhammar, M. Moliner and P. Serna, *Nat. Commun.*, 2025, **16**, 7451.
25 J.-D. Grunwaldt and B. S. Clausen, *Top. Catal.*, 2002, **18**, 37–43.
26 V. Chandra, E. A. J. F. Peters and J. A. M. Kuipers, *Chem. Eng. J.*, 2020, **385**, 123641.
27 B. Harrington, Z. Ye, L. Signor and A. D. Pickel, *ACS Nanosci. Au*, 2024, **4**, 30–61.
28 T. Hartman, R. G. Geitenbeek, G. T. Whiting and B. M. Weckhuysen, *Nat. Catal.*, 2019, **2**, 986–996.
29 T. S. Jacobs, T. P. van Swieten, S. J. W. Vonk, I. P. Bosman, A. E. M. Melcherts, B. C. Janssen, J. C. L. Janssens, M. Monai, A. Meijerink, F. T. Rabouw, W. van der Stam and B. M. Weckhuysen, *ACS Nano*, 2023, **17**, 20053–20061.
30 Z. Ye, D. K. Bommidi and A. D. Pickel, *Adv. Opt. Mater.*, 2023, **11**, 2300824.
31 D. W. Groefsema, F. T. Rabouw, M. Boele, A. P. van Bavel and B. M. Weckhuysen, *Chem. Methods*, 2025, **5**, e202400044.
32 R. Vogel, D. W. Groefsema, M. A. van den Bulk, T. S. Jacobs, P. T. Prins, F. T. Rabouw and B. M. Weckhuysen, *ACS Appl. Mater. Interfaces*, 2025, **17**, 21215–21222.
33 R. G. Geitenbeek, A. E. Nieuwelink, T. S. Jacobs, B. B. V. Salzmann, J. Goetze, A. Meijerink and B. M. Weckhuysen, *ACS Catal.*, 2018, **8**, 2397–2401.
34 C. Liu, B. Qiao and T. Zhang, *JACS Au*, 2024, **4**, 4129–4140.
35 F. Mahnaz, A. Iovine and M. Shetty, *Chem. Sci.*, 2025, **16**, 10106–10118.
36 A. G. Dixon, *Chem. Eng. Sci.*, 2017, **168**, 156–177.
37 B. Partopour and A. G. Dixon, *Chem. Eng. J.*, 2019, **377**, 119738.
38 G. Chabot, R. Guilet, P. Cognet and C. Gourdon, *Chem. Eng. Sci.*, 2015, **127**, 72–83.
39 J. Bremer, K. H. G. Rätze and K. Sundmacher, *AIChE J.*, 2016, **63**, 23–31.
40 Z. Xie, B. Yan, L. Zhang and J. G. Chen, *Ind. Eng. Chem. Res.*, 2017, **56**, 1360–1364.
41 N. M. Schweitzer, R. Gounder and R. M. Rioux, *Addressing Rigor and Reproducibility in Thermal, Heterogeneous Catalysis*, Zenodo, 2024.